THE JOURNAL OF PHYSICAL CHEMISTRY Letters

Physical Insights into Chemistry, Catalysis, and Interfaces

Competing Activation and Deactivation Mechanisms in Photodoped Bismuth Oxybromide Nanoplates Probed by Single-Molecule Fluorescence Imaging

Meikun Shen, Tianben Ding, Jiang Luo, Che Tan, Khalid Mahmood, Zheyu Wang, Dongyan Zhang, Rohan Mishra, Matthew D Lew, and Bryce Sadtler

J. Phys. Chem. Lett., **Just Accepted Manuscript** • DOI: 10.1021/acs.jpclett.0c01237 • Publication Date (Web): 09 Jun 2020

Competing Activation and Deactivation Mechanisms in Photodoped Bismuth Oxybromide Nanoplates Probed by Single-Molecule Fluorescence Imaging

Meikun Shen[1], Tianben Ding[2], Jiang Luo[1], Che Tan[3], Khalid Mahmood[1], Zheyu Wang[4], Dongyan Zhang[1], Rohan Mishra[5,4], Matthew D. Lew[2,4], Bryce Sadtler[1,4]*

[1] Department of Chemistry, Washington University, St. Louis, Missouri 63130

[2] Department of Electrical and Systems Engineering, Washington University, St. Louis, Missouri 63130

[3] Department of Energy, Environmental & Chemical Engineering, Washington University, St. Louis, Missouri 63130

[4] Institute of Materials Science & Engineering, Washington University, St. Louis, Missouri 63130

[5] Department of Mechanical Engineering & Materials Science, Washington University, St. Louis, Missouri 63130

Abstract

Oxygen vacancies in semiconductor photocatalysts play several competing roles, serving to both enhance light absorption and charge separation of photoexcited carriers as well as act as recombination centers for their deactivation. In this Letter, we show that single-molecule fluorescence imaging of a chemically activated fluorogenic probe can be used to monitor changes in the photocatalytic activity of bismuth oxybromide (BiOBr) nanoplates in situ during the light-induced formation of oxygen vacancies. We observe that the specific activities of individual nanoplates for the photocatalytic reduction of resazurin first increase and then progressively decrease under continuous laser irradiation. Ensemble structural characterization, supported by electronic-structure calculations, shows that irradiation increases the concentration of surface oxygen vacancies in the nanoplates, reduces Bi ions, and creates donor defect levels within the band gap of the semiconductor particles. These combined changes first enhance photocatalytic activity by increasing light absorption at visible wavelengths. However, high concentrations of oxygen vacancies lower the photocatalytic activity both by introducing new relaxation pathways that promote charge recombination before photoexcited electrons can be extracted and by weakening binding of resazurin to the surface of the nanoplates.

TOC graphic

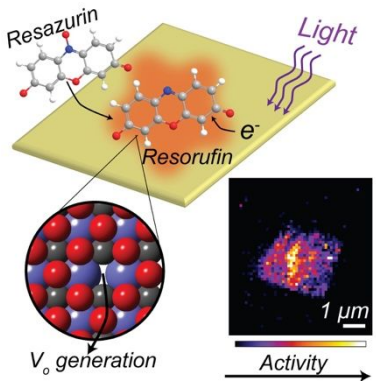

Introduction

Semiconducting metal oxides that harvest solar photons to perform redox reactions are promising materials for generating chemical fuels from sunlight. However, the efficiency of metal oxide photocatalysts are restricted by their low absorption of visible light and low charge-carrier mobility. Oxygen vacancies have been shown to enhance the photocatalytic activity of several metal oxide photocatalysts, including tungsten oxide,[1-3] titanium oxide,[4-12] and bismuth oxyhalides.[13-23] The observed increase in activity for these different materials has been attributed to stronger absorption of visible light,[1, 4-6, 14, 17-18, 20, 24-25] the introduction of mid-gap defect states,[8, 13, 16-19, 24-25] improved charge carrier separation,[5-7, 13-14, 18-20, 22, 24-26] the introduction of preferential adsorption sites for reactant molecules,[1, 3, 7, 14-15, 17, 20-23, 26], or any combination of these effects. The interplay between changes in the electronic structure and surface composition induced by oxygen vacancies and the resulting photocatalytic activity is complex. For example, the hydrogenation of TiO_2 introduces oxygen vacancies in the crystal lattice. While this treatment strongly enhances absorption of visible light below the band gap of pristine TiO_2, it leads to limited photocatalytic activity using visible light alone.[4-5, 7-12] Furthermore, when oxygen vacancies are present in high concentration in hydrogenated TiO_2, the photocatalytic activity has been observed to decrease.[6, 8-12, 26] Prior studies have focused on how systematic variations in the average concentration of oxygen vacancies affect the resulting photocatalytic activity of an ensemble of particles.[6, 8, 12, 21, 23] However, as oxygen vacancies can be created or destroyed photochemically,[13, 15-16, 18, 20-21, 23, 27-29] the balance between different activating and deactivating mechanisms changes during photocatalysis.

Herein, we demonstrate that single-molecule fluorescence microscopy in combination with ensemble characterization and electronic-structure calculations can resolve how oxygen vacancy

concentration affects the activity of BiOBr photocatalysts. We used the fluorogenic probe resazurin, which can be reduced to the highly fluorescent product resorufin,[30-35] to image individual photocatalytic reactions on the surface of single BiOBr nanoplates. Laser irradiation both excites electrons into the conduction band of BiOBr, leading to chemical activation of the probe, and creates oxygen vacancies in the nanoplates. Through single-molecule localization of individual reaction events,[3, 30-44] we tracked changes in the activity of each BiOBr nanoplate in situ as the concentration of oxygen vacancies increased. We show that low concentrations of oxygen vacancies enhance the activity of BiOBr while higher concentrations lead to a decrease in activity. As BiOBr has potential applications in energy conversion and environmental remediation including solar water splitting,[23, 45] CO_2 reduction,[20] N_2 fixation,[17, 22] and the degradation of pollutants,[13-14, 16, 18-19] our results reveal that new passivation schemes are needed to inhibit the formation of high concentrations of oxygen vacancies during photocatalysis.

Results and Discussion

BiOBr nanoplates were synthesized using a hydrothermal method.[46] The details of the synthesis are provided in the Supporting Information. The nanoplates have edge lengths that varied from 1 to 3 micrometers based on scanning electron microscopy (SEM, see Figure 1a). Figure S1 shows the height profile of a single nanoplate with a thickness of 15 nm. Figure 1b shows a high-resolution transmission electron microscope (TEM) image of a nanoplate. The interplanar spacing matches the (110) lattice plane of BiOBr, which indicates the basal facet is the (001) plane.[19, 28] An x-ray diffraction (XRD) pattern of the nanoplates (Figure S2) matched the standard pattern for tetragonal BiOBr (PDF # 04-002-3609). The layered crystal structure, depicted in Figure 1c, was also confirmed by Raman spectroscopy (Figure S3).[18-19, 21, 28, 47] An

absorption spectrum of the BiOBr powder measured using an integrating sphere shows an absorption edge near 420 nm (2.95 eV, see Figure S4), matching previous reports for the band gap of BiOBr.[18, 28, 48-49]

Ultraviolet illumination has been used to introduce oxygen vacancies in bismuth oxyhalide (i.e., BiOCl and BiOBr) particles.[13, 15-16, 18, 20-21, 23, 27] We used x-ray photoelectron spectroscopy (XPS) and Raman spectroscopy to monitor changes in the surface composition and structure of the BiOBr nanoplates following illumination in the presence of the sacrificial reductant, hydroxylamine (NH_2OH). XPS of the initial nanoplates in the binding region for O 1s electrons showed a peak at 530.0 eV corresponding to oxygen within the BiOBr crystal as well as a shoulder peak near 531.5 eV. The shoulder peak has been previously attributed to oxygen-containing adsorbents that bind to metal ions exposed by oxygen vacancies.[13, 19-20, 22-25] We also observed a small shoulder peak at higher binding energy to the Bi^{3+} peak in the Bi 4f spectrum, indicating the presence of Bi^{5+} (Figure 1d).[19, 24-25, 28, 50-51] Figure 1d, e show XPS before and after photodoping using simultaneous excitation from 405- and 561-nm lasers sent through the objective of an inverted optical microscope at the same irradiance used for single-molecule imaging as described below (9 W/cm^2 for 405 nm and 245 W/cm^2 for 561 nm at the sample). The nanoplates were first drop cast onto a silicon substrate and annealed at 400°C for 15 minutes to improve film adhesion (the annealing process did not lead to observable changes by XPS). An aqueous solution of NH_2OH (1 μM) was then added onto the substrate. Focused laser irradiation of the sample on a microscope led to both the disappearance of the contribution from Bi^{5+} and the appearance of peaks at lower binding energy in the Bi 4f spectrum, corresponding to the formation of metallic Bi on the surface of the nanoplates (Figure 1d).[16-18, 21-23, 27, 51] At the same time, the shoulder peak at higher binding energy in the O 1s region increased in intensity with

irradiation time. The combined changes in XPS after irradiating the samples show that the photochemical reduction of bismuth ions is charge-compensated by an increase in the concentration of surface oxygen vacancies (Figure 1e).

While XPS showed changes in surface composition, there was no change in the bulk crystal structure of the nanoplates after laser irradiation as evidenced by Raman spectroscopy (Figure S7). Since a small sample area (~ 8100 μm^2) was illuminated by the microscope, we also photodoped BiOBr nanoplates suspended in solution using a 405-nm LED (irradiance = 8.3 mW/cm^2 at the sample) to further characterize changes in their structure and optical properties. There was no obvious change in the structure or morphology of the nanoplates evidenced by XRD (Figure S2), Raman (Figure S3), and TEM (Figure S6) after photodoping in solution. Furthermore, the peak widths in the XRD pattern of the sample after solution-phase photodoping were the same as those in the initial pattern indicating the absence of lattice strain. However, an absorbance spectrum of the photodoped nanoplates possessed an absorbance tail from 400 to 600 nm below the band gap of BiOBr (Figure S4); this sub-band gap tail has previously been attributed to the presence of oxygen vacancies in BiOBr.[14-18, 20-24]

We propose the following mechanism to account for changes in surface composition observed by XPS following irradiation. Photons with energies above the band gap of BiOBr promote electrons from the valence band into the conduction band (reaction 1). Photoexcited electrons reduce bismuth cations, which are charge compensated by the formation of oxygen vacancies (reaction 2). The concomitant disappearance of the Bi^{5+} signal and appearance of the Bi^0 signal observed by XPS indicates that Bi^{5+} ions are preferentially reduced before Bi^{3+} ions. NH_2OH acts as a sacrificial reductant to maintain charge neutrality in the nanoplates. NH_2OH is

first oxidized to HNO (reaction 3),[52] which is unstable and can be further oxidized to a number of different products (e.g., N_2, N_2O, NO_2, or NO_2^-).[30, 52-54]

$$BiOBr \xrightarrow{h\nu} e_{CB}^- + h_{VB}^+ \quad (1)$$

$$BiOBr + xH_2O + 2xe^- \rightarrow BiO_{1-x}Br + 2xOH^- \quad (2)$$

$$2xNH_2OH + 4xh_{VB}^+ \rightarrow 2xHNO + 4xH^+ \quad (3)$$

To determine how the surface compositional changes induced by photodoping altered the electronic structure of the nanoplates, we performed ultraviolet photoelectron spectroscopy (UPS) and absorbance spectroscopy after irradiating colloidal suspensions of nanoplates for different amounts of time. Based on changes in UPS, the Fermi level of the semiconductor nanoplates shifted to more negative potentials (i.e., closer to the vacuum level) as the photodoping time increased (Figure S8). This change is consistent with the reaction mechanism described in equations 1-3, where the reduction of bismuth ions creates donor defect levels that push the Fermi level toward the conduction band edge. Similar changes in the Fermi level have been previously observed when oxygen vacancies are introduced into BiOCl and BiOBr.[14, 19, 22, 24] As the sub-band gap absorption tail also significantly increased in intensity with increasing irradiation time, we could not quantitatively measure the change in optical band gap using Tauc plots (Figure S9). Qualitatively, the absorption onset shifted to lower energies with increasing irradiation time, indicating a decrease in the band gap of the photodoped nanoplates.

To rationalize these changes in electronic structure, we used density-functional theory (DFT) to calculate the density of states (DOS) for both a defect-free BiOBr crystal (Figure S10) and one that contained 1.4% oxygen vacancies (Figure S11).[16, 20-21, 24] An occupied, mid-gap defect band comprised of Bi 6p states is formed after introducing an oxygen vacancy into a 71-atom BiOBr supercell. Figure S12 compares the calculated absorption spectra of BiOBr supercells

without and with the oxygen vacancy. We find a strong additional peak at energies lower than the band gap due to the mid-gap states introduced by Bi-dangling bonds, which shows that the defect states are optically active and allow dipole-allowed transitions to the empty conduction band. Based on the changes in UPS and the experimental and calculated optical absorption spectra, photodoping increases absorption at longer wavelengths by introducing donor defect states within the band gap. Electrons in these defect states can be excited into the conduction band using visible light (Scheme 1).

To monitor, in situ, how changes in the surface composition and DOS impact the photocatalytic activity of BiOBr, we used resazurin as a chemically activated fluorogenic probe. Photoexcited electrons in the conduction band of BiOBr reduce resazurin to generate the highly fluorescent product, resorufin. The resazurin/resorufin couple has previously been used to study reactions (photo)catalyzed by Au[30-33, 53] and TiO_2.[34-35] At the ensemble level, irradiating a solution containing BiOBr nanoplates, resazurin, and NH_2OH produced fluorescence spectra that matched the spectrum of resorufin[55] and increased in intensity with longer illumination times (Figure S13). While both the initial and photodoped BiOBr samples could activate resazurin when irradiated with a 405-nm LED (i.e., above the band gap of BiOBr), photodoped samples could also generate resorufin using a 566-nm LED (Figure S14), in agreement with the sub-band gap photoactivity predicted by DFT.

Single-molecule fluorescence microscopy provides the ability to image individual reaction events on the surface of catalyst particles using fluorogenic probes, such as the resazurin/resorufin redox couple employed here.[3, 30-44] This technique has been used to study photocatalytic and photoelectrochemical reactions catalyzed by semiconductor particles including TiO_2,[34-35, 37-40] $BiVO_4$,[41] $W_{18}O_{49}$,[3] and CdS[42] as well as plasmonic Au nanoparticles.[30-

[32, 43] Changes in activity due to passivation or restructuring of the catalyst surface can be monitored by counting the number and distribution of fluorescence bursts (i.e., reaction events) over time.[3, 30-31, 33, 40-41] Quantitative information on the catalytic process, including rate and equilibrium constants for elementary steps, can be obtained by fitting the number and distribution of fluorescence bursts to models developed for single-molecule kinetics.[30-31, 33-35, 37-39, 41-43]

To prepare samples for single molecule fluorescence microscopy, dilute suspensions of the BiOBr nanoplates were spin coated on glass coverslips and annealed at 400°C for 15 minutes. A solution of resazurin (typically 40 nM in phosphate buffer with pH 7.4 and 1 μM NH_2OH as a sacrificial reductant) was then added onto each coverslip. Imaging was performed using total internal reflection fluorescence (TIRF) illumination in a wide-field microscope similar to our previous studies on $W_{18}O_{49}$ nanowires (see the SI for further details).[3] A 405-nm laser was used to photoexcite the BiOBr nanoplates, and a 561-nm laser was used to excite resorufin molecules generated on the surface of the photocatalyst. Figure 2a shows the detection of individual fluorescence intensity bursts within a 1×1 μm^2 region on the surface of a single BiOBr nanoplate. Fluorescence bursts were only detected when both BiOBr and resazurin were present. As described further below, we attribute the turn-on of each fluorescence burst to the generation of resorufin on the surface of the nanoplate and the turn-off to its desorption from the surface. Once a resorufin molecule desorbs from the surface, it is no longer detected in TIRF imaging.

Through single-turnover counting of reaction events, we constructed maps showing spatial variations in activity across the surface of individual BiOBr nanoplates. Figure 2c shows an activity map generated by imaging fluorescence bursts for 30 minutes in which the color scale represents the number of bursts detected within each accumulation bin (120×120 nm). The localization precision for capturing individual fluorescent bursts was 22 nm (Figure S15).

Notably, even along the basal (001) facets of the nanoplates there are significant variations in activity. The nanoplate in Figure 2c has a hotspot in the middle with high numbers of reaction events (i.e., 30 bursts per bin) across several neighboring bins. However, other regions are completely inactive. While this nanoplate exhibited higher activity in the middle, other nanoplates displayed hot spots near their edges (See Figures S16 through S21 for additional examples). Previous work using the photodeposition of metal salts as an ex situ method to map the extraction of photoexcited carriers in BiOBr nanoplates has shown that the spatial preference for interfacial electron transfer depends sensitively both on the method used to synthesize the particles and the solution pH used for photodeposition.[56-57] Our in situ method of imaging the extraction of photoexcited electrons reveals heterogeneous reactivity patterns among different nanoplates prepared in the same batch.

Prior to photodoping, fluorescence bursts were only observed when using simultaneous 405-nm and 561-nm laser illumination (Figure 2c). After photodoping colloidal suspensions of nanoplates using a 405-nm LED for 30 minutes, fluorescence intensity bursts under the microscope could also be observed when using only 561-nm excitation (Figure 2e). The single-molecule activity of the photodoped BiOBr nanoplates at this wavelength is consistent with their enhanced absorption in the visible region (see Figure S4) and the photoactivity measured using ensemble fluorescence spectra (Figure S14). Furthermore, the number of bursts was similar when using either dual 405-nm and 561-nm laser illumination (1005 bursts detected in Figure 2d) or only 561-nm illumination (888 bursts detected in Figure 2e). Figure S17 provides additional examples of photodoped BiOBr nanoplates under the two imaging conditions. Similar sub-band gap photoactivity for the reduction of resazurin has been observed in Sb-doped TiO_2 nanorods.[34, 40]

Laser irradiation during single-molecule imaging changes the activity of the nanoplates. To monitor these changes, activity maps consisting of 2500 frames (50 ms exposure, ~ 2 minutes of recording) were constructed at different time points during continuous irradiation using dual laser excitation (i.e., 405 and 561 nm). Figure 3a-c shows a time-sequence of activity maps for the same nanoplate in Figure 2b-c with start times of 0, 5, and 15 minutes. The spatial distribution of the active regions changes continuously during photodoping. The specific activity (i.e., the number of fluorescence bursts per unit time and per lateral area) during the first 2 minutes for this nanoplate was 35 μm^{-2}-min^{-1}. After 5 minutes of irradiation, the specific activity increased to 72 μm^{-2}-min^{-1}, and after 15 minutes of irradiation, it decreased to 39 μm^{-2}-min^{-1} (Figure 3d). Longer irradiation times led to a further decrease in the specific activity. Figure 3d compares the changes in specific activity of the nanoplate shown in Figure 3a-c to the change in average specific activity for 23 nanoplates. While there is a distribution in the initial activity among different nanoplates (the error bars show the standard deviation in activity at each irradiation time), the same trends in activity with irradiation time are observed (i.e., initial increase in specific activity followed by a progressive decrease). The 7 most active nanoplates each had a specific activity (measured over 35 minutes of imaging) that was at least 20% higher than the average specific activity of the 23 particles measured. Activity maps for one of these nanoplates at different times are shown Figure 3e-h; the most active nanoplates each contained one or two hot spots with high activity that developed during the initial stages of photodoping. Additional examples of the changes in activity for individual nanoplates are shown in Figures S18, S19, and S20. We also irradiated samples using dual 405- and 561-nm illumination for 5 minutes and then switched to only 561-nm illumination for single-molecule imaging. After the first five minutes

of photodoping, the nanoplates still showed a progressive decrease in specific activity over time using only the visible excitation wavelength (see Figures S21 and S22).

The dependence of photocatalytic activity on substrate concentration (i.e., resazurin) enables further quantification of how the degree of photodoping changes the kinetics of product formation. We photodoped samples of BiOBr nanoplates for different periods of time using dual laser excitation in the presence of NH_2OH (1 μM), switched solutions to one containing both resazurin (5 to 60 nM) and NH_2OH (1 μM), and performed single-molecule imaging (see the SI for additional details). For each photodoping time and resazurin concentration, we measured the specific activity of 21 different nanoplates. Figure 4a shows that the average specific activity first increases and then saturates as the concentration of resazurin increases. While nanoplates that were photodoped for 5 minutes possess the highest specific activities, the saturation in activity is observed for all photodoping times. This saturation behavior has been previously observed for single-molecule catalysis using Au nanoparticles[30-31] and TiO_2 microcrystals,[37-38] and has been described using a Langmuir-Hinshelwood model for surface reactions (Scheme 1a). In this model, the adsorption of the substrate molecule (resazurin) is fast and in quasi-equilibrium relative to its conversion to the product (resorufin):

$$v = \frac{\gamma_{eff} K_{ad}[Res]}{1 + K_{ad}[Res]} \qquad (4)$$

In equation 4, v is the specific activity of the nanoplate, K_{ad} is the equilibrium constant for adsorption of resazurin onto the nanoplate, $[Res]$ is concentration of resazurin in solution, and γ_{eff} is the effective rate constant for product formation on a single nanoplate (combining all reaction sites on the nanoplate). Fitting the concentration dependence of specific activity to equation 4 provides the change in the interparticle-averaged value of γ_{eff} as a function of the

photodoping time. The initial value for γ_{eff} of 56 ± 29 μm^{-2}-min^{-1} (average ± standard deviation for 21 nanoplates) first increased to 271 ± 86 μm^{-2}-min^{-1} after 5 minutes of photodoping and then decreased to 159 ± 43 μm^{-2}-min^{-1} after 15 minutes of photodoping. On the other hand, the interparticle-averged value of K_{ad} progressively decreased from an initial value of 0.087 ± 0.007 nM^{-1} (average ± standard deviation for 21 nanoplates) to 0.044 ± 0.020 nM^{-1} after 5 minutes of photodoping and then to 0.023 ± 0.010 nM^{-1} after 15 minutes.

The on-time for each fluorescence burst, τ_{on}, characterizes the residence time of a resorufin molecule on the surface of the nanoplate after its formation. For each nanoplate, the distribution of on-times for all fluorescence bursts was fit to an exponential decay (see Figure S15e for an example) to extract a intraparticle-averaged value of τ_{on}. At each photodoping time and resazurin concentration, we measured τ_{on} and its inverse, τ_{on}^{-1}, for 21 nanoplates to determine an interparticle-averaged value, $<\tau_{on}^{-1}>$. The values of $<\tau_{on}^{-1}>$ were independent of the resazurin concentration and showed only a weak dependence on the photodoping time (Figure 4b). If the on-time for fluorescent bursts represented the transformation of resazurin to a non-fluorescent species, such as dihydro-resorufin,[58-59] then $<\tau_{on}^{-1}>$ would be expected to depend on both the resazurin concentration and the photodoping time (see the SI for additional discussion). Thus, we assign $<\tau_{on}^{-1}>$ to the rate constant for the self-dissociation of resorufin from the surface of the nanoplate, k_d, which will be independent of resazurin concentration when the adsorption of resazurin is fast relative to its conversion.[30-31, 37-38]

$$<\tau_{on}^{-1}>= k_d \qquad (5)$$

For photodoping times of 0, 5, and 15 minutes, the values of k_d were 37 ± 1, 42 ± 1, and 46 ± 1 s^{-1}.

The combination of ex situ structural characterization and in situ single-molecule imaging enables us to rationalize how photodoping controls the photocatalytic of the BiOBr nanoplates. Photodoping increases the absorption of visible light in the nanoplates, which enhances their photocatalytic activity during the initial stages of photodoping (Scheme 1b, left). Both ensemble and single-molecule fluorescence measurements show that green light is able to excite electrons into the conduction band in photodoped nanoplates. Our DFT calculations indicate the visible-light activity arises from mid-gap donor levels created by oxygen vacancies. However, as the density of defect states increases, as discussed in the following paragraph, and their distribution of energies within the band gap widens, new relaxation pathways become available for photoexcited charges that promote charge recombination rather than interfacial charge transfer (Scheme 1b, right).[60] Thus, we attribute the progressive decrease in specific activity after the first 5 minutes of photodoping to charge recombination pathways becoming increasingly dominant. These results reveal that, similar to hydrogenated TiO_2,[6, 8-12, 26] high concentrations of oxygen vacancies in BiOBr lead to a reduction in photocatalytic activity.

The photoinduced changes in surface composition affect binding of both reactant and product to the nanoplates, which are reflected in the changes in the equilibrium constant for substrate adsorption, K_{ad}, and the rate constant for product dissociation, k_d. XPS shows that the surfaces of the initial BiOBr nanoplates contain Bi^{5+} ions which are reduced to Bi^{3+} to compensate for the creation of oxygen vacancies. However, prolonged irradiation can lead to the deposition of metallic Bi and release of Br^- from the surface layer.

$$BiOBr + H_2O + 3e^- \xrightarrow{h\nu} Bi + Br^- + 2OH^- \quad (6)$$

As the bulk structure of the nanoplates remains the same after irradiation (compare XPS in Figure 1d to Raman spectra in Figure S7), these compositional changes are limited to the surface of the

nanoplates. The decrease in K_{ad} and increase in k_d reveal that photodoping decreases the activation barrier for desorption of both substrate and product molecules. In the Langmuir-Hinshelwood model,[30-31, 37-38] weaker binding of the substrate molecule leads to a lower turnover rate for product formation. We note that these trends in surface properties are averaged over all sites on the nanoplates. Thus, while the spatial heterogeneity in activity across each nanoplate suggests there are different types of adsorption sites, the overall effect of photodoping is to weaken binding to the surface.

In summary, the ability to vary the concentration of oxygen vacancies through photodoping enabled us to monitor in situ how this type of defect changes the photocatalytic activity of individual BiOBr nanoplates. Through single-molecule counting of photocatalytic reactions on individual nanoplates, we show how nanoscale spatial variations in activity evolve with irradiation time. By correlating super-resolution activity maps with ex situ structural characterization, we attribute the initial enhancement in activity to photoexcited carriers created with visible photons. The progressive decrease in activity at longer irradiation times is the result of both increased competition between charge recombination and charge extraction as well as weaker binding of resazurin to the surface of the nanoplates. While previous studies have shown that the presence of oxygen vacancies can enhance the ensemble photocatalytic activity of BiOBr particles,[13-23] our results demonstrate that the concentration of this defect must be carefully controlled to maintain this enhanced activity. Surface passivation schemes that inhibit the creation of oxygen vacancies during photocatalysis could minimize deactivation of the photocatalyst over prolonged irradiation times. The application of single-molecule imaging to monitor changes in activity can be extended to other semiconductors where oxygen vacancies (or other defects) are introduced or filled in situ through chemical or photochemical treatments.

Figure captions

Figure 1. (a) SEM image of two BiOBr nanoplates. (b) High-resolution TEM image of a BiOBr nanoplate near its edge. (c) The layered crystal structure of BiOBr used in DFT calculations. Bi atoms are purple, oxygen atoms are red, and bromine atoms are brown. (d, e) X-ray photoelectron spectra of films of BiOBr nanoplates before and after laser irradiation showing the binding energy regions for (d) Bi 4f and (e) O 1s electrons. The top traces in each panel show a film annealed on a silicon substrate before photodoping, the middle traces show a film after 5 minutes of laser irradiation using 405-nm and 561-nm lasers, and the bottom traces show a film after 15 minutes of laser irradiation. The dashed blue, red, and green lines for each trace in panel (d) show the deconvolution of the peaks into contributions from Bi(V) (blue lines), Bi(III) (red lines), and Bi metal (green lines). The dashed red and blue lines for each trace in panel (e) show the deconvolution of the peaks into contributions from oxygen within the BiOBr crystal (red lines) and surface-adsorbed, oxygen-containing species (blue lines).

Figure 2. (a) Trajectory of photons in a 1×1 μm^2 region detected during the photocatalytic conversion of resazurin to resorufin on a single BiOBr nanoplate under dual 405-nm and 561-nm laser excitation recorded at an exposure time of 50 ms. (b) Diffraction-limited fluorescence image of the same BiOBr nanoplate in (a). (c) Super-resolution activity map of the same BiOBr nanoplate shown in (b) produced by localizing the positions of all fluorescence bursts detected over a 30-minute period. The color scale below (c) corresponds to the number of fluorescence bursts for each 120×120 nm bin, and the white scale bar is 1 μm. (d, e) Super-resolution activity maps of a different BiOBr nanoplate that was first photodoped in solution using a 405-nm LED

prior to fluorescence imaging (see SI for details). (d) Activity map of the nanoplate using dual 405-nm and 561-nm laser excitation. (e) Activity map of the same nanoplate using only 561-nm laser excitation. The activity maps in (d) and (e) correspond to 2500 frames with a 50 ms exposure time (i.e., 2.08 minutes) to minimize photoinduced changes. The color scale below (e) corresponds to the number of fluorescence bursts per 120×120 bin and applies to both (d) and (e). The white scale bars are each 1 μm. The insets in (d) and (e) show diffraction-limited fluorescence images for each excitation condition, and the scale bars in the insets are each 2 μm.

Figure 3. Super-resolution activity maps of two BiOBr nanoplates under dual 405-nm and 561-nm laser irradiation with photodoping times of (a, e) 0, (b, f) 5, and (c, g) 15 minutes. Each activity map was reconstructed from a video collected for 2500 frames with a 50 ms exposure time (i.e., 2.08 minutes). The color scales below each row correspond to the number of fluorescence bursts per bin and apply to (a-c) and (e-g), respectively. The white scale bars are each 1 μm. The insets in (a-c) and (e-g) show diffraction-limited fluorescence images for each time frame. The scale bars in the insets are each 2 μm. (d) Specific activity of the BiOBr nanoplate shown in (a-c) (red circles) and the average specific activity for 23 different BiOBr nanoplates (black squares) at different photodoping times. (h) Specific activity of the BiOBr nanoplate shown in (e-g) (red circles) and the average specific activity (black squares). The error bars in (d) and (h) represent the standard deviation in activity at each time point, and the lines between points are guides for the eye.

Figure 4. Concentration dependence of single-molecule activity. (a) Dependence of the specific activity on resazurin concentration at different laser-irradiation times. The solid lines are fits to

equation 4. (b) Dependence of $< \tau_{on}^{-1} >$ on resazurin concentration obtained from the same nanoplates in (a). Each data point represents the average of 21 nanoplates. The error bars show the standard deviation across particles.

Scheme 1. (a) Scheme showing the absorption of a substrate molecule resazurin (S) onto the surface of a BiOBr nanoplate, its conversion into the product resorufin (P) and subsequent dissociation from the surface. (b) Scheme showing the band structures for BiOBr nanoplates containing either a low (left) or high (right) concentration of oxygen vacancies. CB = conduction band, and VB = valence band.

Associated content.

Acknowledgements.

This material is based upon work supported by the National Science Foundation (NSF) under grant no. CHE-1753344 to B.S, and under grant no. ECCS-1653777 to M.D.L. R.M. acknowledges NSF for support through DMREF Grant 1729787. Acknowledgment is made to the donors of the American Chemical Society Petroleum Research Fund for partial support of this research (award # PRF58165-DNI10). Computational resources were provided by the Extreme Science and Engineering Discovery Environment (XSEDE), which is supported by NSF grant ACI-1548562. Electron microscopy, atomic force microscopy, and x-ray photoelectron spectroscopy were performed at the Institute of Materials Science & Engineering at Washington University. X-ray diffraction was performed in the Department of Earth and Planetary Sciences at Washington University. The authors thank S. Singamaneni for use of his Raman spectrometer.

Supporting Information Available: Experimental details on the synthesis of bismuth oxybromide nanoplates, methods used to photodope them, and characterization of their structure, morphology, and optical properties before and after photodoping; experimental details on the preparation of samples and instrumentation for single-molecule fluorescence microscopy, analysis and processing of super-resolution images, and computational methods; supporting discussion of the on-times of fluorescent bursts and their interpretation; supporting tables providing the conditions used to photodope different BiBOr samples; supporting figures providing characterization of different BiOBr samples by AFM, XRD Raman spectroscopy, absorption spectroscopy, XPS, TEM, and UPS, calculated density of states and calculated optical spectra for BiOBr crystals with and without oxygen vacancies, ensemble fluorescence spectra showing the activation of resazurin by different BiOBr samples, quantitative characterization of resazurin blinking events, additional super-resolution activity maps of BiOBr nanoplates before and after photodoping and with and without 405-nm laser excitation. This material is available free of charge via the internet at http://pubs.acs.org

Author information.

*email: sadtler@wustl.edu

Conflicts of interest. The authors declare no competing financial interest.

References

1. Zhang, N.; Li, X.; Ye, H.; Chen, S.; Ju, H.; Liu, D.; Lin, Y.; Ye, W.; Wang, C.; Xu, Q.; Zhu, J.; Song, L.; Jiang, J.; Xiong, Y., Oxide Defect Engineering Enables to Couple Solar Energy into Oxygen Activation. *Journal of the American Chemical Society* **2016,** *138*, 8928-8935.
2. Meng, J.; Lin, Q.; Chen, T.; Wei, X.; Li, J.; Zhang, Z., Oxygen Vacancy Regulation on Tungsten Oxides with Specific Exposed Facets for Enhanced Visible-Light-Driven Photocatalytic Oxidation. *Nanoscale* **2018,** *10*, 2908-2915.
3. Shen, M.; Ding, T.; Hartman, S. T.; Wang, F.; Krucylak, C.; Wang, Z.; Tan, C.; Yin, B.; Mishra, R.; Lew, M. D.; Sadtler, B., Nanoscale Colocalization of Fluorogenic Probes Reveals the Role of Oxygen Vacancies in the Photocatalytic Activity of Tungsten Oxide Nanowires. *ACS Catalysis* **2020,** *10*, 2088-2099.
4. Zuo, F.; Wang, L.; Wu, T.; Zhang, Z.; Borchardt, D.; Feng, P., Self-Doped Ti^{3+} Enhanced Photocatalyst for Hydrogen Production under Visible Light. *Journal of the American Chemical Society* **2010,** *132*, 11856-11857.
5. Chen, X.; Liu, L.; Yu, P. Y.; Mao, S. S., Increasing Solar Absorption for Photocatalysis with Black Hydrogenated Titanium Dioxide Nanocrystals. *Science* **2011,** *331*, 746-750.
6. Sinhamahapatra, A.; Jeon, J.-P.; Yu, J.-S., A New Approach to Prepare Highly Active and Stable Black Titania for Visible Light-Assisted Hydrogen Production. *Energy & Environmental Science* **2015,** *8*, 3539-3544.
7. Khan, M. M.; Ansari, S. A.; Pradhan, D.; Ansari, M. O.; Han, D. H.; Lee, J.; Cho, M. H., Band Gap Engineered TiO_2 Nanoparticles for Visible Light Induced Photoelectrochemical and Photocatalytic Studies. *Journal of Materials Chemistry A* **2014,** *2*, 637-644.
8. Xue, J.; Zhu, X.; Zhang, Y.; Wang, W.; Xie, W.; Zhou, J.; Bao, J.; Luo, Y.; Gao, X.; Wang, Y.; Jang, L.-y.; Sun, S.; Gao, C., Nature of Conduction Band Tailing in Hydrogenated Titanium Dioxide for Photocatalytic Hydrogen Evolution. *ChemCatChem* **2016,** *8*, 2010-2014.

9. Zhang, K.; Park, J. H., Surface Localization of Defects in Black TiO_2: Enhancing Photoactivity or Reactivity. *The Journal of Physical Chemistry Letters* **2017,** *8*, 199-207.

10. Naldoni, A.; Altomare, M.; Zoppellaro, G.; Liu, N.; Kment, Š.; Zbořil, R.; Schmuki, P., Photocatalysis with Reduced TiO_2: From Black TiO_2 to Cocatalyst-Free Hydrogen Production. *ACS Catalysis* **2019,** *9*, 345-364.

11. Cushing, S. K.; Meng, F.; Zhang, J.; Ding, B.; Chen, C. K.; Chen, C.-J.; Liu, R.-S.; Bristow, A. D.; Bright, J.; Zheng, P.; Wu, N., Effects of Defects on Photocatalytic Activity of Hydrogen-Treated Titanium Oxide Nanobelts. *ACS Catalysis* **2017,** *7*, 1742-1748.

12. Liu, N.; Zhou, X.; Nguyen, N. T.; Peters, K.; Zoller, F.; Hwang, I.; Schneider, C.; Miehlich, M. E.; Freitag, D.; Meyer, K.; Fattakhova-Rohlfing, D.; Schmuki, P., Black Magic in Gray Titania: Noble-Metal-Free Photocatalytic H_2 Evolution from Hydrogenated Anatase. *ChemSusChem* **2017,** *10*, 62-67.

13. Ye, L.; Zan, L.; Tian, L.; Peng, T.; Zhang, J., The {001} Facets-Dependent High Photoactivity of BiOCl Nanosheets. *Chemical Communications* **2011,** *47*, 6951-6953.

14. Guan, M.; Xiao, C.; Zhang, J.; Fan, S.; An, R.; Cheng, Q.; Xie, J.; Zhou, M.; Ye, B.; Xie, Y., Vacancy Associates Promoting Solar-Driven Photocatalytic Activity of Ultrathin Bismuth Oxychloride Nanosheets. *Journal of the American Chemical Society* **2013,** *135*, 10411-10417.

15. Zhao, K.; Zhang, L.; Wang, J.; Li, Q.; He, W.; Yin, J. J., Surface Structure-Dependent Molecular Oxygen Activation of BiOCl Single-Crystalline Nanosheets. *Journal of the American Chemical Society* **2013,** *135*, 15750-15753.

16. Li, H.; Shi, J.; Zhao, K.; Zhang, L., Sustainable Molecular Oxygen Activation with Oxygen Vacancies on the {001} Facets of BiOCl Nanosheets under Solar Light. *Nanoscale* **2014,** *6*, 14168-14173.

17. Li, H.; Shang, J.; Ai, Z.; Zhang, L., Efficient Visible Light Nitrogen Fixation with BiOBr Nanosheets of Oxygen Vacancies on the Exposed {001} Facets. *Journal of the American Chemical Society* **2015,** *137*, 6393-6399.

18. Wang, X.-j.; Zhao, Y.; Li, F.-t.; Dou, L.-j.; Li, Y.-p.; Zhao, J.; Hao, Y.-j., A Chelation Strategy for in-Situ Constructing Surface Oxygen Vacancy on {001} Facets Exposed BiOBr Nanosheets. *Scientific Reports* **2016,** *6*, 24918.

19. Wang, H.; Yong, D.; Chen, S.; Jiang, S.; Zhang, X.; Shao, W.; Zhang, Q.; Yan, W.; Pan, B.; Xie, Y., Oxygen-Vacancy-Mediated Exciton Dissociation in BiOBr for Boosting Charge-Carrier-Involved Molecular Oxygen Activation. *Journal of the American Chemical Society* **2018,** *140*, 1760-1766.

20. Wu, J.; Li, X.; Shi, W.; Ling, P.; Sun, Y.; Jiao, X.; Gao, S.; Liang, L.; Xu, J.; Yan, W.; Wang, C.; Xie, Y., Efficient Visible-Light-Driven CO_2 Reduction Mediated by Defect-Engineered BiOBr Atomic Layers. *Angewandte Chemie International Edition* **2018,** *57*, 8719-8723.

21. Mao, C.; Cheng, H.; Tian, H.; Li, H.; Xiao, W.-J.; Xu, H.; Zhao, J.; Zhang, L., Visible Light Driven Selective Oxidation of Amines to Imines with BiOCl: Does Oxygen Vacancy Concentration Matter? *Applied Catalysis B: Environmental* **2018,** *228*, 87-96.

22. Xue, X.; Chen, R.; Chen, H.; Hu, Y.; Ding, Q.; Liu, Z.; Ma, L.; Zhu, G.; Zhang, W.; Yu, Q.; Liu, J.; Ma, J.; Jin, Z., Oxygen Vacancy Engineering Promoted Photocatalytic Ammonia Synthesis on Ultrathin Two-Dimensional Bismuth Oxybromide Nanosheets. *Nano Letters* **2018,** *18*, 7372-7377.

23. Li, H.; Shang, J.; Zhu, H.; Yang, Z.; Ai, Z.; Zhang, L., Oxygen Vacancy Structure Associated Photocatalytic Water Oxidation of BiOCl. *ACS Catalysis* **2016,** *6*, 8276-8285.

24. Li, J.; Wu, X.; Pan, W.; Zhang, G.; Chen, H., Vacancy-Rich Monolayer BiO_{2-x} as a Highly Efficient UV, Visible, and Near-Infrared Responsive Photocatalyst. *Angewandte Chemie International Edition* **2018,** *57*, 491-495.

25. Li, J.; Wang, J.; Zhang, G.; Li, Y.; Wang, K., Enhanced Molecular Oxygen Activation of Ni^{2+}-Doped BiO_{2-x} Nanosheets under UV, Visible and Nnear-Infrared Irradiation: Mechanism and DFT Study. *Applied Catalysis B: Environmental* **2018,** *234*, 167-177.

26. Zhang, G.; Yang, X.; He, C.; Zhang, P.; Mi, H., Constructing a Tunable Defect Structure in TiO_2 for Photocatalytic Nitrogen Fixation. *Journal of Materials Chemistry A* **2020,** *8*, 334-341.

27. Ye, L.; Deng, K.; Xu, F.; Tian, L.; Peng, T.; Zan, L., Increasing Visible-Light Absorption for Photocatalysis with Black BiOCl. *Physical Chemistry Chemical Physics* **2012,** *14*, 82-85.

28. Wu, D.; Yue, S.; Wang, W.; An, T.; Li, G.; Ye, L.; Yip, H. Y.; Wong, P. K., Influence of Photoinduced Bi-Related Self-Doping on the Photocatalytic Activity of BiOBr Nanosheets. *Applied Surface Science* **2017,** *391*, 516-524.

29. Tao, X.; Shi, W.; Zeng, B.; Zhao, Y.; Ta, N.; Wang, S.; Adenle, A. A.; Li, R.; Li, C., Photoinduced Surface Activation of Semiconductor Photocatalysts under Reaction Conditions: A Commonly Overlooked Phenomenon in Photocatalysis. *ACS Catalysis* **2020,** *10*, 5941-5948.

30. Xu, W.; Kong, J. S.; Yeh, Y.-T. E.; Chen, P., Single-Molecule Nanocatalysis Reveals Heterogeneous Reaction Pathways and Catalytic Dynamics. *Nature Materials* **2008,** *7*, 992-996.

31. Zhou, X.; Xu, W.; Liu, G.; Panda, D.; Chen, P., Size-Dependent Catalytic Activity and Dynamics of Gold Nanoparticles at the Single-Molecule Level. *Journal of the American Chemical Society* **2010,** *132*, 138-146.

32. Zou, N.; Chen, G.; Mao, X.; Shen, H.; Choudhary, E.; Zhou, X.; Chen, P., Imaging Catalytic Hotspots on Single Plasmonic Nanostructures Via Correlated Super-Resolution and Electron Microscopy. *ACS Nano* **2018,** *12*, 5570-5579.

33. Chen, T.; Zhang, Y.; Xu, W., Single-Molecule Nanocatalysis Reveals Catalytic Activation Energy of Single Nanocatalysts. *Journal of the American Chemical Society* **2016,** *138*, 12414-12421.

34. Xu, W.; Jain, P. K.; Beberwyck, B. J.; Alivisatos, A. P., Probing Redox Photocatalysis of Trapped Electrons and Holes on Single Sb-Doped Titania Nanorod Surfaces. *Journal of the American Chemical Society* **2012,** *134*, 3946-3949.

35. Sambur, J. B.; Chen, T.-Y.; Choudhary, E.; Chen, G.; Nissen, E. J.; Thomas, E. M.; Zou, N.; Chen, P., Sub-Particle Reaction and Photocurrent Mapping to Optimize Catalyst-Modified Photoanodes. *Nature* **2016,** *530*, 77-80.

36. Roeffaers, M. B. J.; Sels, B. F.; Uji-i, H.; Schryver, F. C. D.; Jacobs, P. A.; Vos, D. E. D.; Hofkens, J., Spatially Resolved Observation of Crystal-Face-Dependent Catalysis by Single Turnover Counting. *Nature* **2006,** *439*, 572-575.

37. Wang, N.; Tachikawa, T.; Majima, T., Single-Molecule, Single-Particle Observation of Size-Dependent Photocatalytic Activity in Au/TiO_2 Nanocomposites. *Chemical Science* **2011,** *2*, 891-900.

38. Tachikawa, T.; Yamashita, S.; Majima, T., Evidence for Crystal-Face-Dependent TiO_2 Photocatalysis from Single-Molecule Imaging and Kinetic Analysis. *Journal of the American Chemical Society* **2011,** *133*, 7197-7204.

39. Tachikawa, T.; Yonezawa, T.; Majima, T., Super-Resolution Mapping of Reactive Sites on Titania-Based Nanoparticles with Water-Soluble Fluorogenic Probes. *ACS Nano* **2013,** *7*, 263-275.

40. Zhang, Y.; Lucas, J. M.; Song, P.; Beberwyck, B.; Fu, Q.; Xu, W.; Alivisatos, A. P., Superresolution Fluorescence Mapping of Single-Nanoparticle Catalysts Reveals Spatiotemporal Variations in Surface Reactivity. *Proceedings of the National Academy of Sciences* **2015,** *112*, 8959-8964.

41. Mao, X.; Liu, C.; Hesari, M.; Zou, N.; Chen, P., Super-Resolution Imaging of Non-Fluorescent Reactions Via Competition. *Nature Chemistry* **2019,** *11*, 687-694.

42. Ha, J. W.; Ruberu, T. P. A.; Han, R.; Dong, B.; Vela, J.; Fang, N., Super-Resolution Mapping of Photogenerated Electron and Hole Separation in Single Metal–Semiconductor Nanocatalysts. *Journal of the American Chemical Society* **2014,** *136*, 1398-1408.

43. Zhou, X.; Andoy, N. M.; Liu, G.; Choudhary, E.; Han, K.-S.; Shen, H.; Chen, P., Quantitative Super-Resolution Imaging Uncovers Reactivity Patterns on Single Nanocatalysts. *Nature Nanotechnology* **2012,** *7*, 237-241.

44. Chen, T.; Dong, B.; Chen, K.; Zhao, F.; Cheng, X.; Ma, C.; Lee, S.; Zhang, P.; Kang, S. H.; Ha, J. W.; Xu, W.; Fang, N., Optical Super-Resolution Imaging of Surface Reactions. *Chemical Reviews* **2017,** *117*, 7510-7537.

45. Di, J.; Chen, C.; Yang, S.-Z.; Ji, M.; Yan, C.; Gu, K.; Xia, J.; Li, H.; Li, S.; Liu, Z., Defect Engineering in Atomically-Thin Bismuth Oxychloride Towards Photocatalytic Oxygen Evolution. *Journal of Materials Chemistry A* **2017,** *5*, 14144-14151.

46. Feng, H.; Xu, Z.; Wang, L.; Yu, Y.; Mitchell, D.; Cui, D.; Xu, X.; Shi, J.; Sannomiya, T.; Du, Y.; Hao, W.; Dou, S. X., Modulation of Photocatalytic Properties by Strain in 2D BiOBr Nanosheets. *ACS Applied Materials & Interfaces* **2015,** *7*, 27592-27596.

47. Zhang, D.; Li, J.; Wang, Q.; Wu, Q., High {001} Facets Dominated BiOBr Lamellas: Facile Hydrolysis Preparation and Selective Visible-Light Photocatalytic Activity. *Journal of Materials Chemistry A* **2013,** *1*, 8622-8629.

48. Ganose, A. M.; Cuff, M.; Butler, K. T.; Walsh, A.; Scanlon, D. O., Interplay of Orbital and Relativistic Effects in Bismuth Oxyhalides: BiOF, BiOCl, BiOBr, and BiOI. *Chemistry of Materials* **2016,** *28*, 1980-1984.

49. Wang, Y.; Shi, Z.; Fan, C.; Wang, X.; Hao, X.; Chi, Y., Synthesis, Characterization, and Photocatalytic Properties of BiOBr Catalyst. *Journal of Solid State Chemistry* **2013,** *199*, 224-229.

50. Antony, R. P.; Baikie, T.; Chiam, S. Y.; Ren, Y.; Prabhakar, R. R.; Batabyal, S. K.; Loo, S. C. J.; Barber, J.; Wong, L. H., Catalytic Effect of Bi^{5+} in Enhanced Solar Water Splitting of Tetragonal $BiV_{0.8}Mo_{0.2}O_4$. *Applied Catalysis A: General* **2016,** *526*, 21-27.

51. Bhachu, D. S.; Moniz, S. J. A.; Sathasivam, S.; Scanlon, D. O.; Walsh, A.; Bawaked, S. M.; Mokhtar, M.; Obaid, A. Y.; Parkin, I. P.; Tang, J.; Carmalt, C. J., Bismuth Oxyhalides: Synthesis, Structure and Photoelectrochemical Activity. *Chemical Science* **2016,** *7*, 4832-4841.

52. Bengtsson, G.; Fronæus, S.; Bengtsson-Kloo, L., The Kinetics and Mechanism of Oxidation of Hydroxylamine by Iron(III). *Journal of the Chemical Society, Dalton Transactions* **2002**, 2548-2552.

53. Alejo, C. J. B.; Fasciani, C.; Grenier, M.; Netto-Ferreira, J. C.; Scaiano, J. C., Reduction of Resazurin to Resorufin Catalyzed by Gold Nanoparticles: Dramatic Reaction Acceleration by Laser or LED Plasmon Excitation. *Catalysis Science & Technology* **2011,** *1*, 1506-1511.

54. Godoi, D. R. M.; Chen, Y.; Zhu, H.; Scherson, D., Electrochemical Oxidation of Hydroxylamine on Gold in Aqueous Acidic Electrolytes: An in Situ SERS Investigation. *Langmuir* **2010,** *26*, 15711-15713.

55. Gomes, A.; Fernandes, E.; Lima, J. L. F. C., Fluorescence Probes Used for Detection of Reactive Oxygen Species. *Journal of Biochemical and Biophysical Methods* **2005,** *65*, 45-80.

56. Guo, Y.; Siretanu, I.; Zhang, Y.; Mei, B.; Li, X.; Mugele, F.; Huang, H.; Mul, G., pH-Dependence in Facet-Selective Photo-Deposition of Metals and Metal Oxides on Semiconductor Particles. *Journal of Materials Chemistry A* **2018,** *6*, 7500-7508.

57. Shi, M.; Li, G.; Li, J.; Jin, X.; Tao, X.; Zeng, B.; Pidko, E. A.; Li, R.; Li, C., Intrinsic Facet-Dependent Reactivity of Well-Defined BiOBr Nanosheets on Photocatalytic Water Splitting. *Angewandte Chemie International Edition* **2020,** *59*, 6590-6595.

58. Xu, W.; Shen, H.; Kim, Y. J.; Zhou, X.; Liu, G.; Park, J.; Chen, P., Single-Molecule Electrocatalysis by Single-Walled Carbon Nanotubes. *Nano Letters* **2009,** *9*, 3968-3973.

59. Wang, X.; Kafizas, A.; Li, X.; Moniz, S. J. A.; Reardon, P. J. T.; Tang, J.; Parkin, I. P.; Durrant, J. R., Transient Absorption Spectroscopy of Anatase and Rutile: The Impact of Morphology and Phase on Photocatalytic Activity. *The Journal of Physical Chemistry C* **2015,** *119*, 10439-10447.

60. Jones, M.; Lo, S. S.; Scholes, G. D., Quantitative Modeling of the Role of Surface Traps in CdSe/CdS/Zns Nanocrystal Photoluminescence Decay Dynamics. *Proceedings of the National Academy of Sciences* **2009,** *106*, 3011-3016.

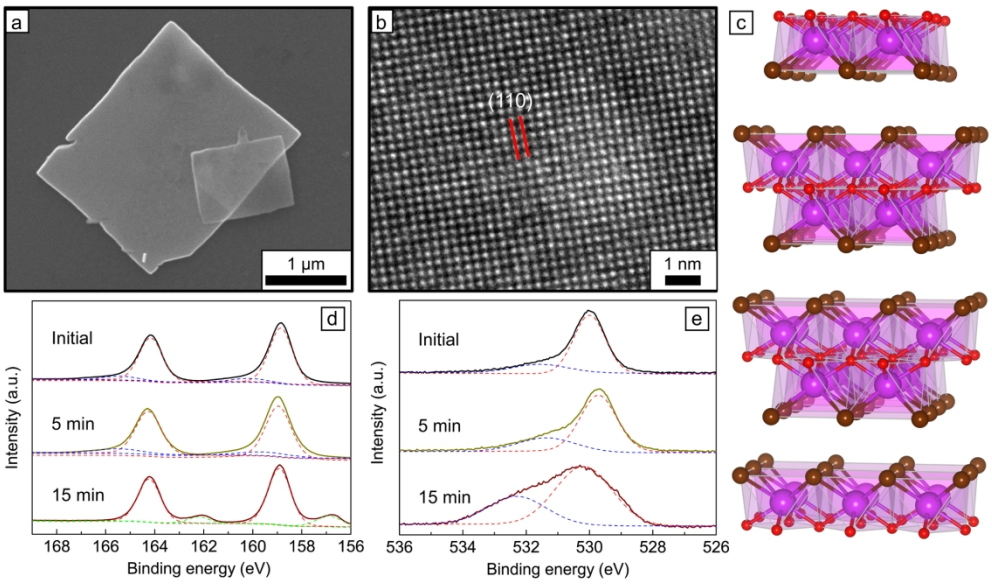

Figure 1

177x103mm (300 x 300 DPI)

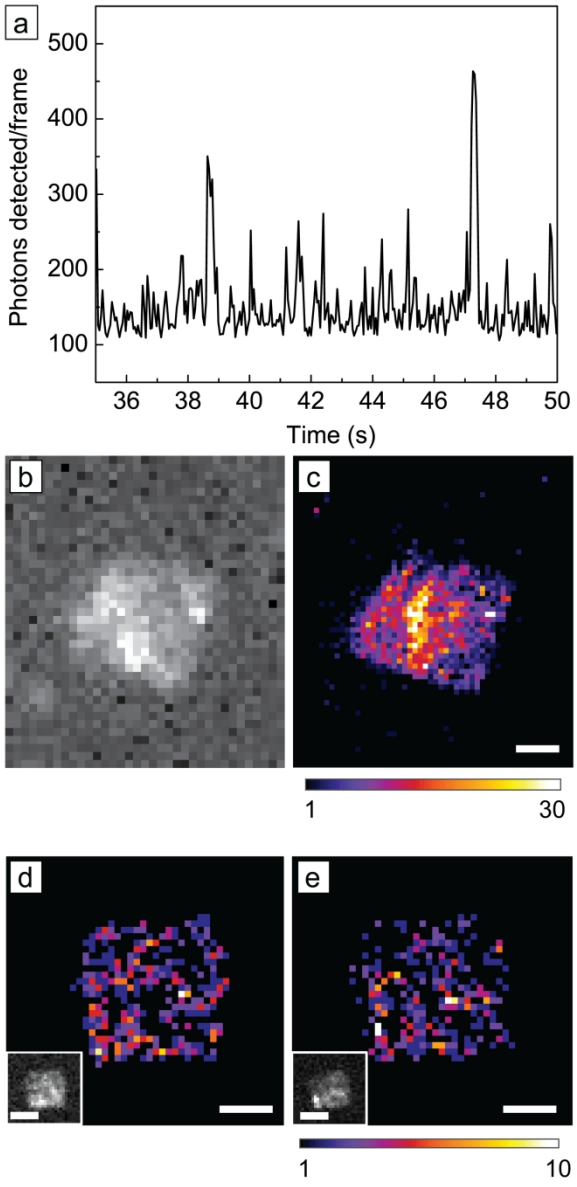

Figure 2

85x175mm (600 x 600 DPI)

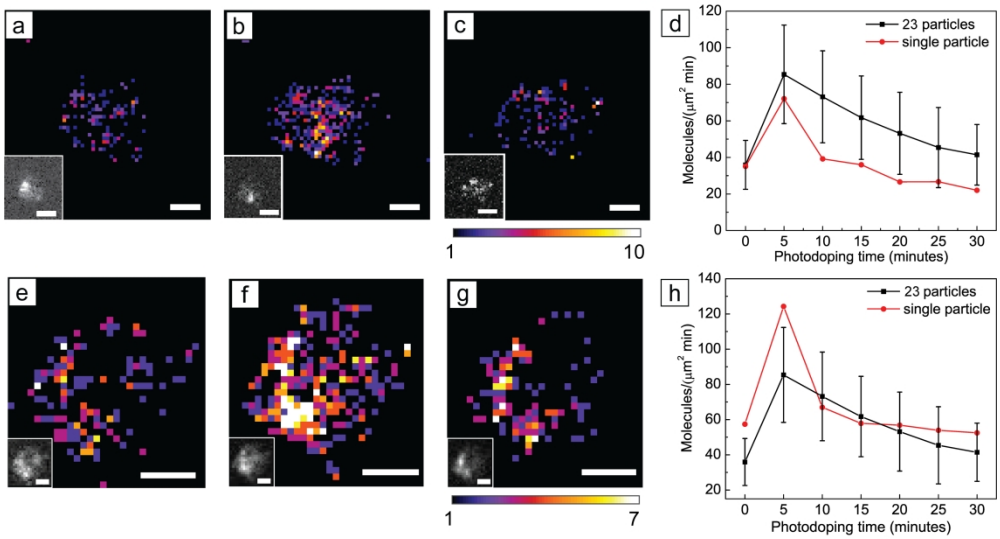

Figure 3

176x96mm (600 x 600 DPI)

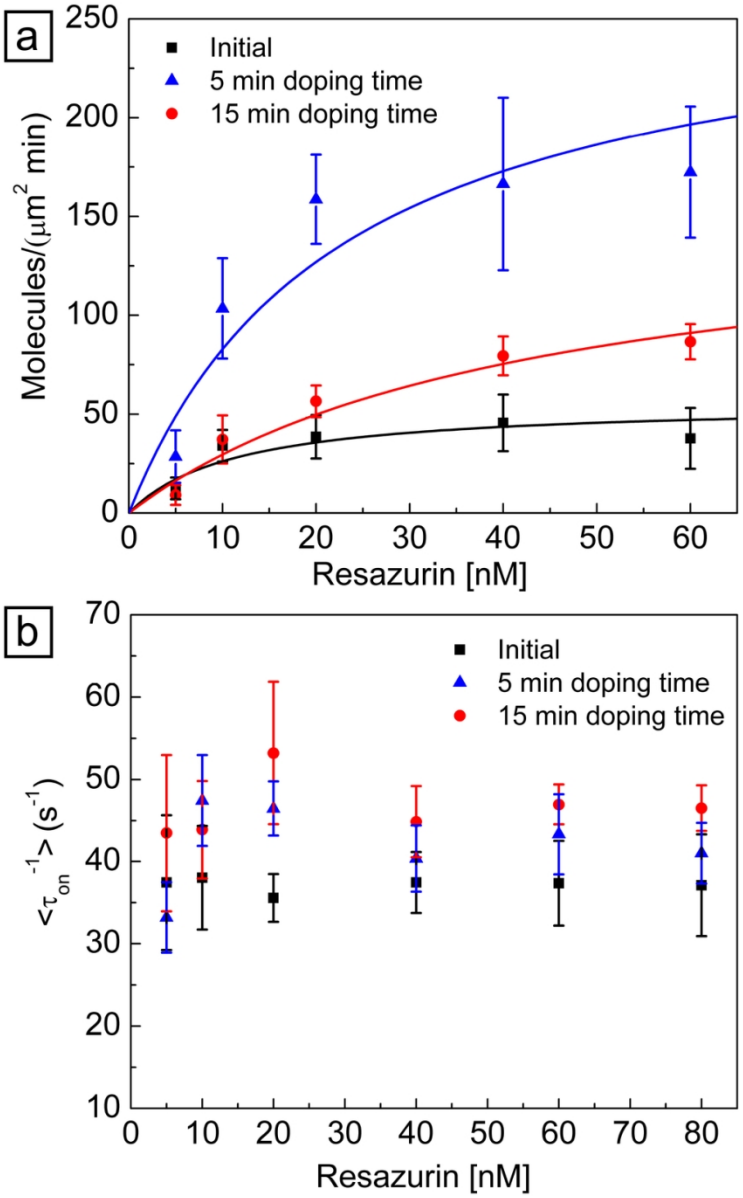

Figure 4

86x138mm (300 x 300 DPI)

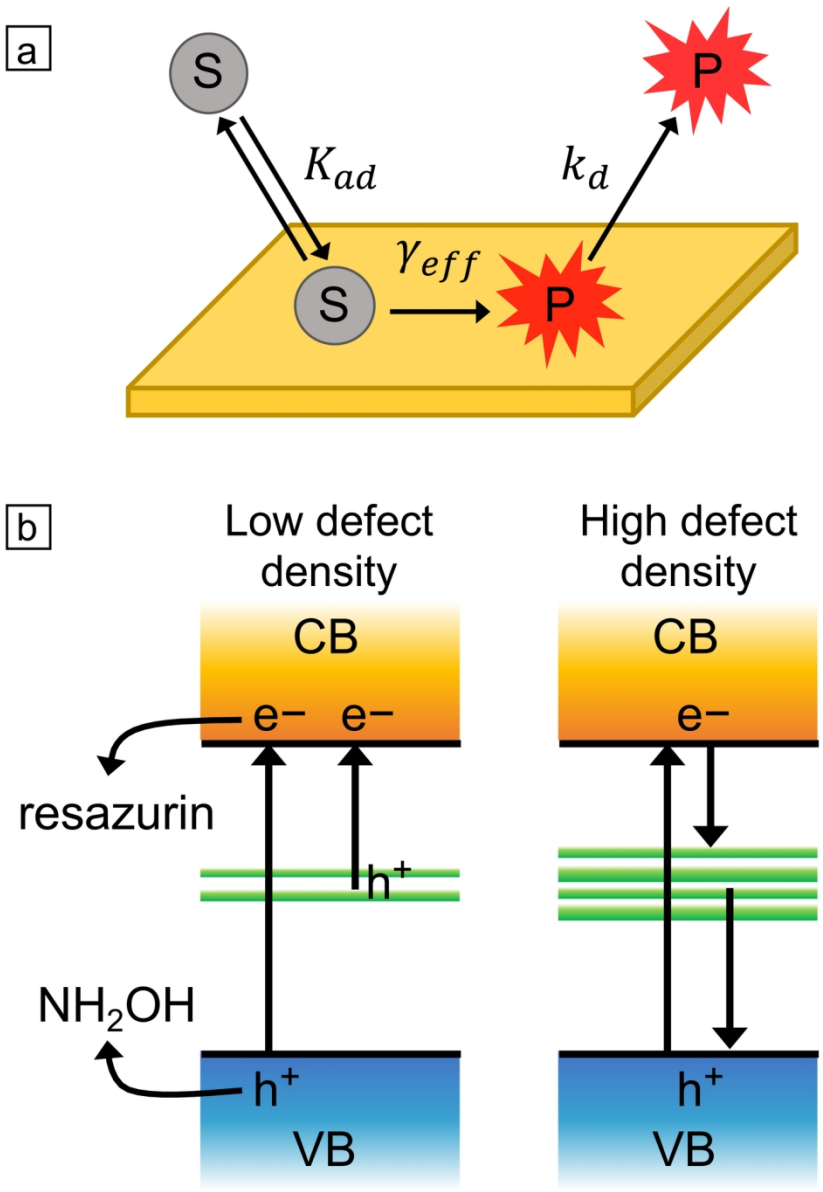

124x176mm (300 x 300 DPI)

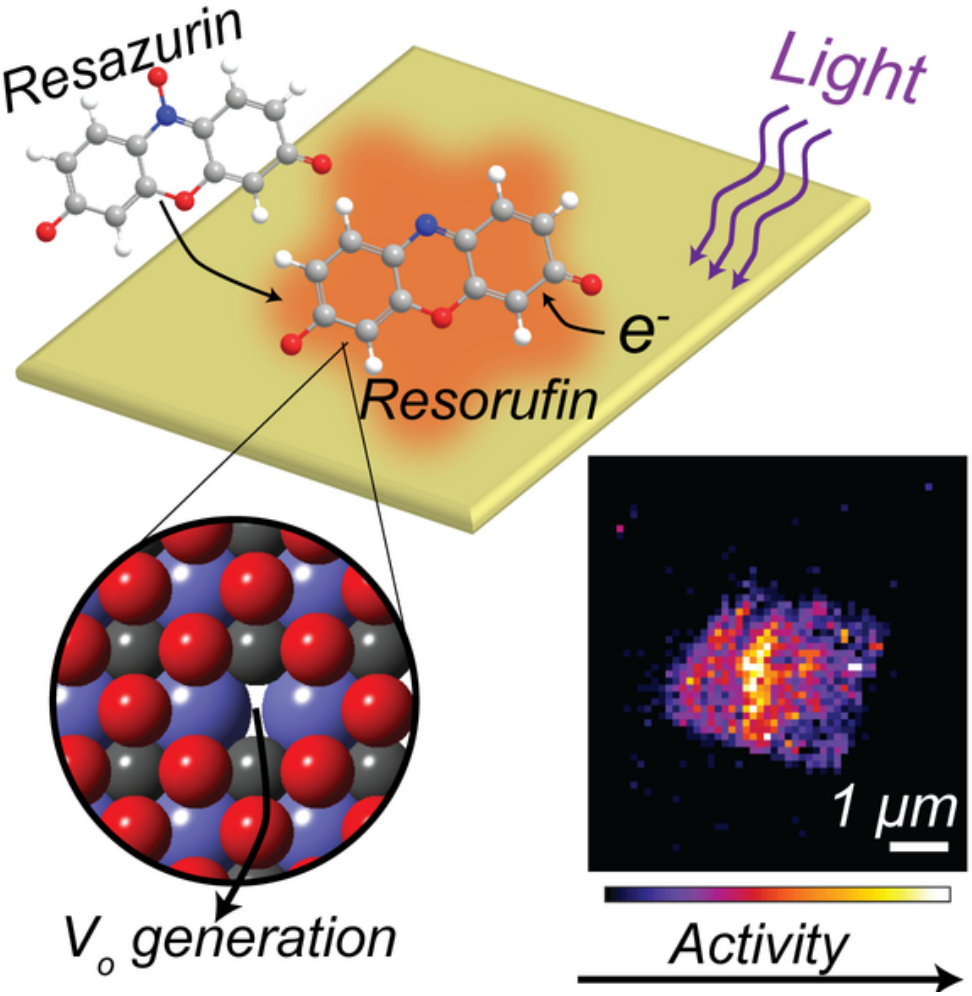

TOC graphic

50x50mm (300 x 300 DPI)